

Kent Academic Repository

Full text document (pdf)

Citation for published version

Ma, Zhengzheng, Tan, Lei, Huang, Haijun, He, Lunhua, Chen, Jie, Lu, Huaile, Deng, Sihao, Yin, Wen, Zhang, Junrong, Tian, Haolai and others (2022) Neutron powder-diraction study of phase transitions in strontium-doped bismuth ferrite: 1. Variation with chemical composition. *Journal of Physics: Condensed Matter* . ISSN 0953-8984. (In press)

DOI

<https://doi.org/10.1088/1361-648X%2Fac6389>

Link to record in KAR

<https://kar.kent.ac.uk/94068/>

Document Version

Author's Accepted Manuscript

Copyright & reuse

Content in the Kent Academic Repository is made available for research purposes. Unless otherwise stated all content is protected by copyright and in the absence of an open licence (eg Creative Commons), permissions for further reuse of content should be sought from the publisher, author or other copyright holder.

Versions of research

The version in the Kent Academic Repository may differ from the final published version.

Users are advised to check <http://kar.kent.ac.uk> for the status of the paper. **Users should always cite the published version of record.**















Enquiries

For any further enquiries regarding the licence status of this document, please contact:

researchsupport@kent.ac.uk

If you believe this document infringes copyright then please contact the KAR admin team with the take-down information provided at <http://kar.kent.ac.uk/contact.html>

Neutron powder-diffraction study of phase transitions in strontium-doped bismuth ferrite: 1. Variation with chemical composition

Zhengzheng Ma ¹, Lei Tan ¹, Haijun Huang ¹, Lunhua He ^{2,3,4}, Jie Chen ^{4,5}, Huaile Lu ^{4,5}, Sihao Deng ^{4,5}, Wen Yin ^{4,5}, Junrong Zhang ^{4,5}, Haolai Tian ^{4,5}, Rong Du ^{4,5}, Donna C Arnold ⁶, Anthony E Phillips ⁷, Martin T Dove ^{1,8,9,7}

¹ Department of Physics, School of Sciences, Wuhan University of Technology, 205 Luoshi Road, Hongshan district, Wuhan, Hubei, 430070, China

² Beijing National Laboratory for Condensed Matter Physics, Institute of Physics, Chinese Academy of Sciences, Beijing 100190, China

³ Songshan Lake Materials Laboratory, Dongguan, Guangdong 523808, China

⁴ Spallation Neutron Source Science Center, Dongguan, Guangdong 523803, China

⁵ Institute of High Energy Physics, Chinese Academy of Sciences, Beijing 100049, China

⁶ School of Physical Sciences, University of Kent, Canterbury, Kent CT2 7NH, United Kingdom

⁷ School of Physical and Chemical Sciences, Queen Mary University of London, Mile End Road, London, E1 4NS, United Kingdom

⁸ College of Computer Science, Sichuan University, Chengdu, Sichuan 610065, China

⁹ School of Mechanical Engineering, Dongguan University of Technology, 1st Daxue Road, Songshan Lake, Dongguan, Guangdong 523000, China

E-mail: martin.dove@icloud.com

Abstract. We report results from a study of the crystal structure of strontium-doped BiFeO₃ using neutron powder diffraction and the Rietveld method. Measurements were obtained over a wide range of temperatures from 300–800 K for compositions between 10–16% replacement of bismuth by strontium. The results show a clear variation of the two main structural deformations – symmetry-breaking rotations of the FeO₆ octahedra and polar ionic displacements that give ferroelectricity – with chemical composition, but relatively little variation with temperature. On the other hand, the antiferromagnetic order shows a variation with temperature and a second order phase transition consistent with the classical Heisenberg model. There is, however, very little variation in the behaviour of the antiferromagnetism with chemical composition, and hence with the degree of the structural symmetry-breaking distortions. We therefore conclude that there is no significant coupling between antiferromagnetism and ferroelectricity in Sr-doped BiFeO₃ and, by extension, in pure BiFeO₃.

1. Introduction

Within the current interest in multiferroic materials, BiFeO₃ has assumed a high level of significance, owing to the fact that it shows both ferroelectricity and antiferromagnetism at room temperature [1, 2]. Many of the key features of BiFeO₃ have been reviewed by Catalan and Scott [3] and Park et al [4]. BiFeO₃ has a typical perovskite structure with octahedral rotation and ferroelectric distortions from a parent high-symmetry cubic structure [5], giving a crystal structure of rhombohedral symmetry [1, 2, 6, 7].

There is a lot of interest in improving the practical properties of BiFeO₃ by chemical doping, to enhance, for example, the chemical and electronic performance [8, 9]. One approach that has been widely explored is to substitute the octahedrally-coordinated Fe³⁺ cations by trivalent transition metals such as Mn³⁺ [10]. There have also been studies of doping on the 12-coordinated Bi³⁺ site by trivalent rare-earth elements [11]. It is also possible to replace the Bi³⁺ cations with a divalent cation, including alkali earth cations [12, 8]. Of interest in this paper is the observation of a composition-induced structural phase transition in Sr²⁺-doped BiFeO₃, apparently to a phase of cubic (sometimes claimed as pseudo-cubic tetragonal) symmetry [13, 14, 15, 16, 17, 18].

Nominally-stoichiometric BiFeO₃ decomposes at temperatures below that for its transitions to higher-symmetry phases (described in Section 2), which means that these have only been accessed experimentally through fast diffraction measurements [1, 6]. To understand the phase transitions in BiFeO₃ and their mechanisms it is necessary to have experimental access to the higher-symmetry phases, and this appears to be feasible with Sr-doped BiFeO₃, with the advantage that we have both temperature and composition as variables. In this paper we present the results from a systematic study of the atomic and magnetic structures of Sr-doped BiFeO₃, Sr_xBi_{1-x}FeO_{3-x/2}.[‡] Using neutron powder diffraction, we study the variation of atomic and magnetic structures with both composition and temperature. We focus on samples with values of x in the range 0.1–0.16, and compare these data with our previous results for a sample with $x = 0$ [7]. In a second paper (in preparation) we will report further measurements obtained in a separate study that will focus more on the variation with temperature at higher concentrations.

In Section 2 of this paper we review some background information on the atomic and magnetic structure of BiFeO₃, with details of the structural instabilities relative to the parent phase of cubic symmetry that give rise to the observed crystal structure. We also review recent work on Sr-doped BiFeO₃. In Section 3 we describe the sample synthesis and the neutron diffraction measurements. Our analysis of the neutron diffraction results are then presented in Section 4. Lattice parameters are analysed in terms of the shear strain that accompanies the cubic–rhombohedral distortion, showing a gradual decrease in strain

[‡] Readers should be aware that in this paper we have two distinct meanings for the variable x , both of which follow convention. Here x denotes the relative concentration of Sr in the chemical formula, but later x also denotes one of the fractional atomic coordinates by which crystal structures are conventionally described.

on increasing Sr content but with much less variation with temperature. The atomic coordinates are analysed in terms of the normal modes associated with the transition from the parent cubic phase to the ferroelectric rhombohedral phase. The variation of the distortions again shows a significant variation with increasing Sr content, with reduction in both the size of the ferroelectric and rotational distortions. The ferroelectric distortion appears to have very little variation with temperature, but a small variation is observed in the rotational distortion. On the other hand, the size of the antiferromagnetic moment with temperature follows a normal dependence on temperature (classical Heisenberg behaviour), with no significant changes associated with Sr content.

The results, as discussed in Section 5, confirm earlier suggestions, either implicit through the presentation of data or made more explicitly, that the coupling between the antiferromagnetism and the two structural distortions – particularly the ferroelectricity – is virtually insignificant in Sr-doped BiFeO₃. Comparison of our work with an analysis of the temperature dependence of the crystal structure of pure BiFeO₃ (Appendix A) leads us to conclude that the same is true in the parent phase too.

2. Background

2.1. BiFeO₃

The nuclear structure of BiFeO₃ at ambient temperature – denoted as the α phase – is that of a classical distorted perovskite structure [1, 2, 7, 20], with polar rhombohedral space group $R3c$, as seen in other oxides such as sodium niobate at low temperature [21]. The crystal structure of α -BiFeO₃ is shown in Figure 1. The Fe³⁺ cations occupy the sites with 6-fold coordination with oxygen, forming a slightly distorted octahedral shape. The Bi³⁺ cations occupy the sites with 12-fold coordination with oxygen, with displacements, relative to the positions of the oxygen atoms, along the 3-fold axis.

The crystal structure of α -BiFeO₃ is derived from the parent cubic perovskite structure (denoted as the γ phase) by two deformations. First is a rotation of the FeO₆ octahedra about the cubic [111] axis, with opposite rotations in alternate (111) layers, as indicated in Figure 1b. This lowers the space group symmetry to the centrosymmetric $R\bar{3}c$, and is accomplished by softening of a normal mode of symmetry R_5^- , giving the structure characterised by the prototypical perovskite LaAlO₃. In Glazer notation [22] this distortion has the symbol $a^-a^-a^-$. The second distortion is the ferroelectric distortion, accomplished by cation and anion displacements along the [111] direction to break the centre of symmetry and thereby lower the symmetry to $R3c$. These distortions are shown in Figure 1a. The transition to the ferroelectric state is accomplished by softening of a normal mode of symmetry Γ_4^- . This ferroelectric distortion also deforms the FeO₆ octahedra, as seen in Figure 1c. It appears that as the Fe cation moves upwards relative to the centre of the octahedron, the Fe–O bonds remain of more-or-less constant length [7], which means that the oxygen atoms above the iron cation are pushed outwards, and the atoms below are pulled inwards. This balance is easy to maintain because the

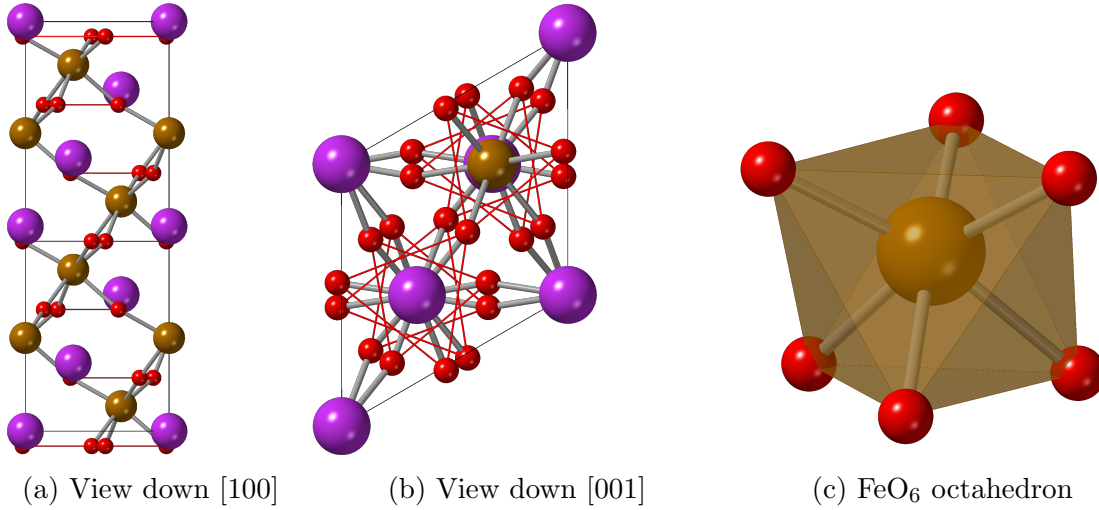


Figure 1: Crystal structure of the rhombohedral α phase of BiFeO₃ (space group $R3c$, using the conventional setting with trigonal unit cell axes), showing bismuth atoms as purple spheres, iron atoms as gold spheres, and oxygen atoms as red spheres, and Fe–O bonds as grey cylinders. a) View down [100]. The horizontal thin red lines connect the three top and bottom atoms within the FeO₆ octahedra. The figure highlights the ferroelectric atomic displacements along [001] (vertical direction), with the O and Bi atoms being displaced in opposite directions from their coplanar arrangement in the non-ferroelectric state (not that in the polar state there is no unique origin for the z axis), and the Fe cations displaced away from the centres of the octahedra. b) View down [001] showing the rotations of FeO₆ octahedra. In this view some distortion of the octahedra can be seen, because without distortion the O atoms near the faces of the unit cell would lie exactly on the faces. c) Perspective view of an FeO₆ octahedron, showing expanded (top) and contracted (bottom) pairs of O₃ triangles. Images were generated using CrystalMaker software [19].

connections between octahedra mean that an expanding O₃ group is directly linked to a contracting O₃ group in the same plane, with no local stresses needing to be generated.

At 1093 K BiFeO₃ undergoes a discontinuous phase transition to a structure of orthorhombic symmetry, centro-symmetric space group $Pbnm$ [1, 23]. This has a different system of FeO₆ octahedral rotations, designated $a^-a^-b^+$ in Glazer notation [22]. Because the space group of the α phase is not a subgroup of the space group of the β phase, the structure of the rhombohedral α phase is better discussed in relationship to the parent cubic phase of space group $Pm\bar{3}m$. The exact identity of this proposed phase, designated as γ , has proven elusive, in part due to thermal instability [6, 24, 25], with contrary indications from diffraction experiments of cubic or orthorhombic symmetry.

The antiferromagnetism of BiFeO₃ is classical G-type [26] on an approximately cubic lattice, with neighbouring spins in each of the three dimensions having opposite orientation [27]. The antiferromagnetic phase transition temperature is around 630 K [11, 27]. There

is an additional long-period spiral magnetisation with weak overall magnetic moment [27, 28, 29, 30], which is presumed [4] to arise from the Dzyaloshinskii–Moriya interaction [31, 32]. This is very hard to observe in neutron powder diffraction measurements except in the highest resolution diffractometers.

The properties of α -BiFeO₃ crystals have been extensively studied by many different methods, as discussed in two earlier review articles [3, 4], but with much work published subsequently. This includes measurements of phonon [33, 34, 35, 36] and spin wave [37] excitations. It was seen that the magnetic excitations behave as conventional spin waves in a regular antiferromagnet over all parts of the Brillouin zone [37]. Some of this work has been focussed on several different aspects of the structural and magnetic phase transitions investigated by various experimental methods [23, 24, 25, 38]. There have also been many simulation studies in support of the experimental work, both with density functional theory (DFT) [39, 40, 41, 42] and force field [43] methods. One aspect of interest has been the effect of the phase transitions on the electronic structure and band gap [42], and another on understanding the complex magnetic structure [30]. Some work has been carried out to understand the magneto-electric coupling [40, 44]. DFT calculations have suggested that the Dzyaloshinskii–Moriya vector that controls the spiral magnetism depends more on the octahedral rotation than on the dielectric polarisation [40]. Other DFT calculations have also suggested that there is a significant variation of the electronic band gap associated with both octahedral rotation and ferroelectric ionic displacements [42]. Studies such as these encourage the suggestion that physical properties may be tuned by chemical doping.

Much work has also been performed on thin films and heterostructures of BiFeO₃ [45, 46, 47, 48], since this is likely to be the main area of applications of multiferroics. For example, there is much recent work on controlling magnetism in epitaxial layers within heterostructures [49, 50, 51], the behaviour of ferroelectric domains [52], and in developing magneto-electrical control of devices [53, 54]. The extent to which such control is enabled by the intrinsic multiferroic coupling – about which we will have some comments below based on the work of this paper – or due to the interactions with other components in the heterostructures is not clear.

2.2. Sr-doped BiFeO₃

As remarked above, there has been considerable work on doped BiFeO₃ [8, 9], investigating both structure [55, 56] and magnetism [57], including doping on either cation site or forming solid solutions such as mixing of BiFeO₃–CaTiO₃ [57] and BiFeO₃–PbTiO₃ [55]. A number of studies have reported the variation of the crystal structure with Sr content at ambient temperature [13, 15, 16, 17, 18]. Generally it is reported that there is a transition from the rhombohedral ferroelectric structure to a phase of either cubic (space group $Pm\bar{3}m$) or tetragonal (space group $P4/mmm$) symmetry. Typically publications show the results of x-ray powder diffraction measurements at ambient temperature, and in some cases the diffraction data were analysed using Rietveld refinement. There are

some inconsistencies within the literature regarding behaviour at specific compositions, but this is not surprising given difficulties in controlling the exact chemical composition during synthesis, in avoiding formation of secondary phases during the synthesis, and from chemical inhomogeneity [13, 14, 18]. Nevertheless, the transition to a phase with a cubic or pseudo-cubic unit cell is consistent between different studies. The Rietveld refinements in $P4/mmm$ have atoms located on special positions equivalent to those in the cubic $Pm\bar{3}m$ structure. We note that there is a lack of studies using neutron powder diffraction with variable temperature; neutron diffraction has the important advantage over x-ray diffraction in that the neutron scattering factors for the different elements are much more similar than they are for x-rays, giving greater sensitivity to the displacements of oxygen atoms.

The same G-type antiferromagnetism seen in BiFeO₃ also appears to exist in Sr-doped BiFeO₃, apparently persisting into the cubic phase [13, 16].

Mössbauer spectroscopy measurements on Sr-doped BiFeO₃ [14] show that the iron cations remain as Fe³⁺ on doping. Therefore to retain charge balance, substitution of trivalent Bi³⁺ cations by divalent Sr²⁺ cations is accompanied by the formation of oxygen vacancies. Thus the chemical formula of Sr-doped BiFeO₃ is best described as Sr_xBi_{1-x}FeO_{3-x/2}.

In this paper we envisage that this background information points to the possibilities of phase transitions on increasing temperature or Sr content from the known $R3c$ ferroelectric structure of BiFeO₃ with antiferromagnetic ordering to structures that are non-magnetic, non-polar and without rotations of the FeO₆ octahedra (that is, with cubic space group $Pm\bar{3}m$). Although in this paper we only see the phase transition involving antiferromagnetic order, we do see significant changes in crystal structure with Sr content that point to the possibility of a phase transition to a cubic structure. Changes with temperature are found to be much weaker.

3. Methods

3.1. Sample preparation

The ceramic samples of Sr-doped BiFeO₃ ceramics for this work were synthesised by a modified Pechini method [58], as used in previous studies [17, 59]. Mixtures of bismuth nitrate pentahydrate, Bi(NO₃)₃·5H₂O, iron nitrate nonahydrate, Fe(NO₃)₃·9H₂O, and strontium nitrate tetrahydrate, Sr(NO₃)₂·4H₂O, of appropriate stoichiometric ratios were dissolved into citric acid solutions with 5% excess bismuth nitrate to compensate for possible bismuth loss during the subsequent sintering process. The solutions were adjusted to a pH value of 7–8 by addition of ammonia. The mixtures were then dried at 150 °C to form gels, which were then ignited to form low-density solids which were easily powdered. These powders were then calcined at 500 °C for 5 hours. The products were ground by hand in an agate bowl for about 2 hours and then pressed into disc wafers. The wafers were sintered at a temperature of 900 °C for 2 hours, and then quenched to

room temperature to minimise the evaporation of bismuth. The wafers were subsequently ground by hand to form fine powders for the neutron diffraction measurements.

In this paper we have used the nominal compositions. It was not possible to refine the composition from Rietveld analysis with sufficient accuracy (requiring accuracy to better than ± 0.01 to be useful) to test the nominal compositions. We consider that the nominal compositions are reasonable for the analysis presented in our paper because we never plot data as a direct function of composition.

Extensive characterisation measurements for an identical suite of samples prepared by the lead author (ZM) have been previously reported [17]. These included dielectric impedance spectroscopy, measurements of dielectric polarisation hysteresis loops, and measurements of magnetisation. This prior work showed that Sr-doped BiFeO₃ prepared using the same method is ferroelectric, and with a divergence of the dielectric susceptibility at a composition of around $x \approx 0.2$ where the crystal structure appears to become of cubic metric.

3.2. Neutron powder diffraction and Rietveld analysis

Neutron powder diffraction measurements were performed on the General Purpose Powder Diffractometer at the China Spallation Neutron Source [60, 61]. The powdered samples of Sr-doped BiFeO₃ were loaded into thin-walled vanadium cans of diameter 9 mm, which were mounted within a cryo-furnace for temperature control. Temperature readings were calibrated against the results of a set of external measurements, but there is some uncertainty in this calibration at the higher temperatures of ± 20 K. This does not significantly affect analysis of trends of data across a wide range of temperatures as reported in the next section. However, we will caution against over-interpretation of the observed magnetic order transition temperatures (see further comments in Section 4.3). Data for refinement were collected for the low-angle (30° scattering angle) and medium-angle (90°) detectors, with recording times of 30 minutes. As is always the case in experiments performed using central facilities, experimental time was limited, and so we were able to collect full suites of data for some compositions only, with sparser sets of data for other compositions. All measurements were performed using the same experimental configuration.

The crystal atomic and magnetic structures were refined by the Rietveld method, using the program GSAS-II [62]. For all compositions investigated here the data appear to be consistent with space group $R3c$, as indicated in previous diffraction studies of Sr-doped BiFeO₃ for the range of compositions studied here [13, 15, 17, 18]. We were unable to find evidence for space group $P4/mmm$ or $Pbnm$ as previously suggested for compositions $x > 0.15$ [13, 15, 18]. The initial lattice parameters and atomic fractional coordinates for space group $R3c$ were taken from our previous work on pure BiFeO₃ [7]. The magnetic structure used was the simple G-type antiferromagnetic structure [26] identified by previous workers, where nearest neighbour spins on the iron cations are of opposite sign [11, 13, 16]. The crystal structure was refined using individual isotropic

atomic displacement parameters. Line shapes were fitted using models for uniaxial size and isotropic microstrain. No attempt was made to measure sample attenuation, and refinement of an absorption coefficient did not give meaningful results.

The full set of refined values of the lattice parameters, atomic fractional coordinates, and average atomic magnetic moment are given in the Supporting Information [63]. An example of the fitting is shown in Figure 2. The fitted diffraction patterns for each composition at the lowest and highest temperatures are given in Figures S1–S20 in the Supporting Information [63].

We remark that the diffraction patterns show four very weak additional peaks. One may be the (110) reflection from the vanadium can (2.15 Å), which is not uncommonly seen in such experiments, and another may be the (111) reflection from aluminium (2.34 Å). A third appears to be the (113) Bragg peak from Fe₂O₃ (2.22 Å) as a secondary phase from the synthesis. The fourth additional peak at 3.22 Å is less easy to assign to a secondary phase with similar confidence. It may be associated with Bi₂Fe₄O₉ as a common secondary phase, but the strong (110) Bragg peak from this material at 5.78 Å is extremely weak if present (outside the range of data used in the Rietveld analysis) leading us to believe this may not be the origin of that peak. Because these peaks are so weak, and where identified represent the very strongest reflections from that phase, we did not account for them as additional phases in the refinements. We would have needed a more extensive set of Bragg peaks from any secondary phases to have been able to include them in the Rietveld refinement.

We also wish to remark that we do not believe that the presence of small sample impurity peaks implies an effect on the physics studied here. The unknown phase is not from a magnetic iron oxide, and thus will not generate local magnetic fields. Moreover, because any secondary phases will be oxides, the effect of their formation on the stoichiometry of the main sample will be weak, because any secondary phases will be formed by both cations and anions and will not deplete the concentration of any one element in the sample phase preferentially.

4. Analysis

4.1. Lattice parameters

We begin our analysis of the structure of Sr-doped BiFeO₃ by considering the behaviour of the lattice parameters. These often give sensitive measurements of lattice strains that accompany structure distortions associated with phase transitions [12, 64, 65], and therefore provide a useful first look at the overall behaviour of the system as a function of both temperature and chemical composition. In the case of the cubic to rhombohedral transition, the strain is associated with stretching the unit cell along the cubic [111] direction, expanding the hexagonal *c* axis relative to the *a* axis. Refined values of lattice parameters for all compositions and temperatures are given in the Supporting Information [63].

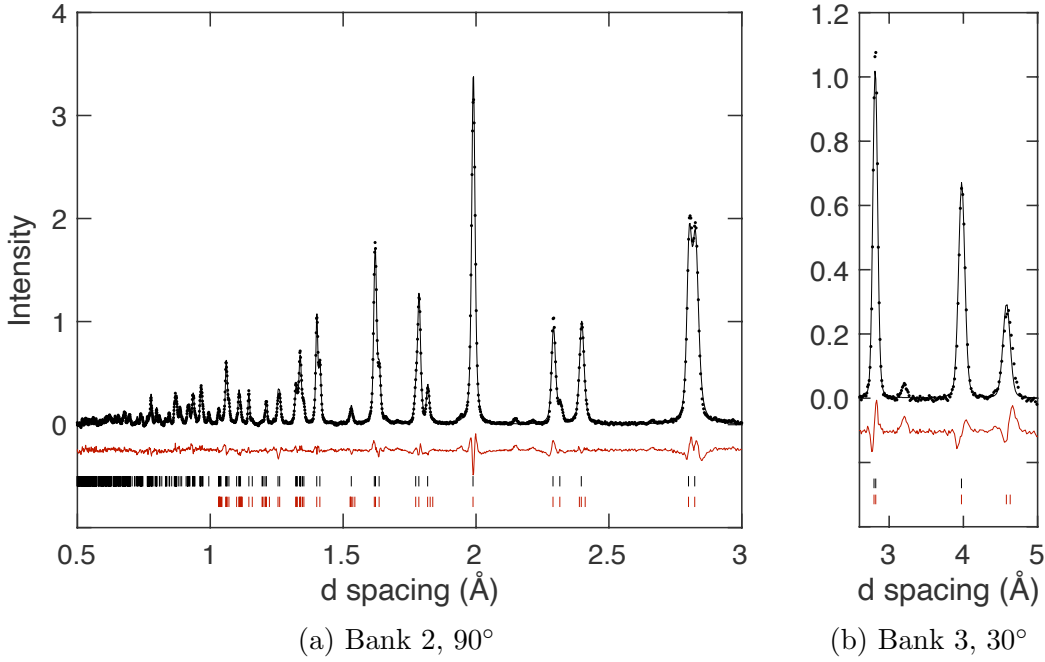


Figure 2: Example of the Rietveld refinement of $\text{Sr}_x\text{Bi}_{1-x}\text{FeO}_{3-x/2}$, $x = 0.1$ at a temperature of 600 K. Data are shown for the two banks of detectors used in the measurement, with their nominal scattering angle. Experimental data, with fitted background subtracted, are shown as points, and the black line represents the fitted diffraction pattern. The red curve represents the difference between observation and calculation. Black tick marks show the positions of the Bragg peaks for nuclear scattering, and the red tick marks show the positions of the Bragg peaks for magnetic scattering. Note the existence of a strong peak of pure magnetic scattering at a time of around 6.9 ms. A few small impurity peaks are seen in this sample; one is a weak Bragg peak from the vanadium can, and others are likely to be from Fe_2O_3 and $\text{Bi}_2\text{Fe}_4\text{O}_9$ secondary phases. Weighted R factors for the two data sets are 6.0% and 7.8% respectively, and profile R factors are 4.6% and 5.7%.

The lattice parameters in the hexagonal setting (a, c) of the space group $R3c$ of Sr-doped BiFeO_3 are related to those of the cubic phase (subscript c) by the relations $a \simeq \sqrt{2}a_c$ and $c \simeq \sqrt{12}a_c$. The variations of the refined values of $a/\sqrt{2}$ and $c/\sqrt{12}$ with temperature for all compositions are shown in Figure 3a. Values of the unit cell volume for different composition are shown in 3b, where volume is scaled to that of the parent cubic unit cell as $a^2c/4\sqrt{3}$. The two lattice parameters show very similar positive thermal expansion, with a linear expansivity $\alpha = a^{-1}\partial a/\partial T \simeq 10 \times 10^{-6} \text{ K}^{-1}$.

The key result from Figure 3a is that the values of a vary only slightly with composition, whereas the values of c decrease significantly in value with an increase in strontium content. There are two competing size effects. Strontium has a larger ionic radius (1.40 Å for Sr^{2+}) than bismuth (1.31 Å for Bi^{3+} , data from the standard Shannon analysis of ionic radii [66]), and therefore increasing Sr content might be expected to

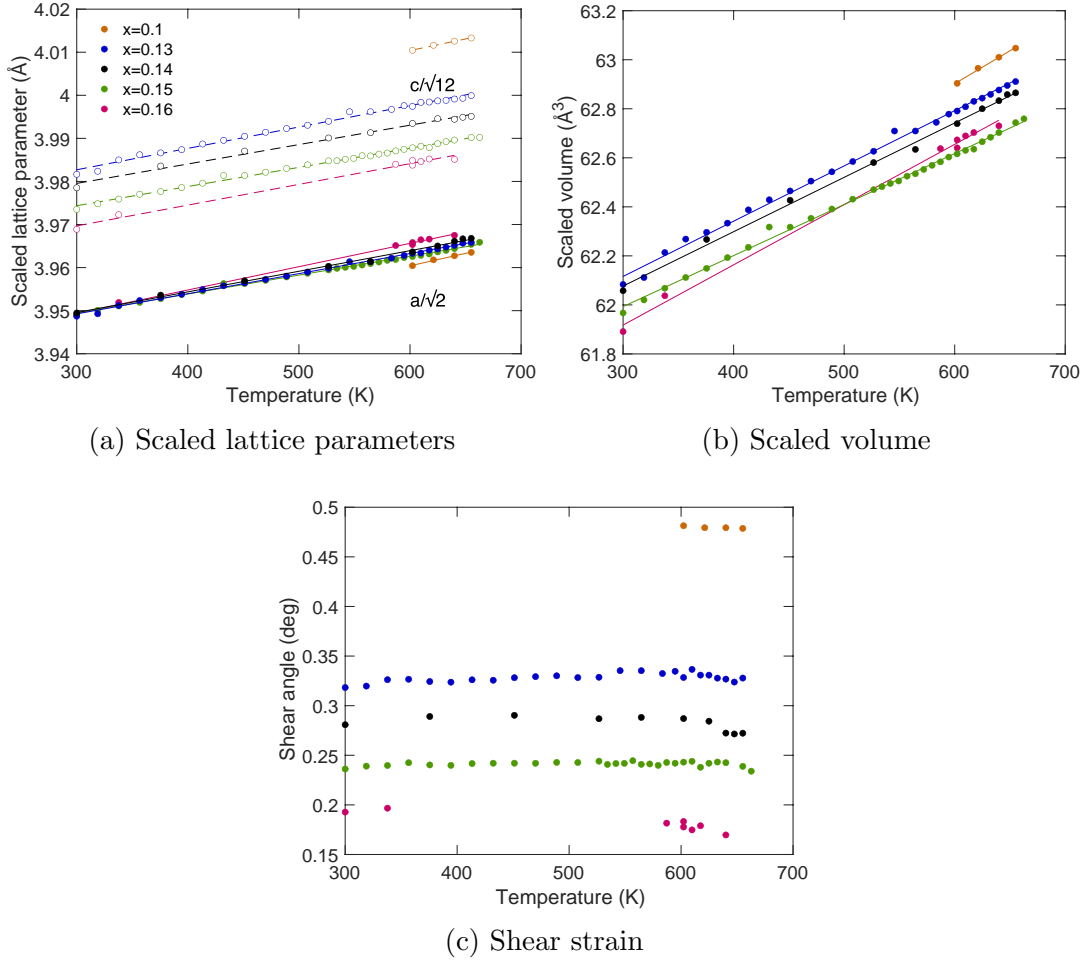


Figure 3: a) Refined values of the lattice parameters of $\text{Sr}_x\text{Bi}_{1-x}\text{FeO}_{3-x/2}$ as functions of measurement temperatures for various compositions x , where closed circles (solid lines) represent values of $a/\sqrt{2}$ and open circles (dashed lines) represent values of $c/\sqrt{12}$. The scaling of lattice parameters is to reduce their values corresponding to those of the parent cubic phase. b) Temperature dependence of the scaled volume of $\text{Sr}_x\text{Bi}_{1-x}\text{FeO}_{3-x/2}$ calculated as $a^2c/4\sqrt{3}$, for various compositions x . c) Temperature dependence of the shear strain of rhombohedral $\text{Sr}_x\text{Bi}_{1-x}\text{FeO}_{3-x/2}$ for various values of x , calculated from the lattice parameters as described in the text. The legend in plot (a) displays the values of composition x for each graph.

increase rather than decrease the volume. On the other hand, replacement of Bi^{3+} by Sr^{2+} leads to a concomitant creation of O^{2-} vacancies (1 vacancy for 2 cation replacements), which should reduce the volume overall. However, if size effects were the most important point, we would expect that the effect would be similar for both a and c , which is not seen in Figure 3a. Instead, we also need to consider the effects of the two structural phase transitions, which may be the dominant effect. We will return to this in Section 4.2.4 below.

As noted above, the transition from cubic to rhombohedral symmetry involves a

Table 1: Representation of the crystallographic Wyckoff positions of atoms in each phase of Sr-doped BiFeO₃, together with our data for $x = 0.13$ at a temperature of 300 K. The position in the $Pm\bar{3}m$ are given with respect to the same rhombohedral unit cell. In the $R3c$ phase the z origin is not defined by symmetry, and we have chosen to place the origin on the Bi atom.

Atom	$R3c$	Experimental	$R\bar{3}c$	$Pm\bar{3}m$
Bi	0, 0, 0	0, 0, 0	0, 0, 0	0, 0, 0
Fe	0, 0, z	0, 0, 0.225	0, 0, 1/4	0, 0, 1/4
O	x, y, z	0.456, 0.017, -0.039	$x, 0, 0$	1/2, 0, 0

shear strain as the lattice expands along the [111] direction. This can be characterised by identifying three nearly-orthogonal vectors in the lattice of the rhombohedral phase that correspond to the three orthogonal basis vectors of the underlying cubic lattice. The angles between these vectors in the rhombohedral structure will give the shear strain as the difference from 90°.

One set of nearly orthogonal vectors of equal length is

$$\begin{aligned}\mathbf{a}' &= (0, a/\sqrt{3}, c/6) \\ \mathbf{b}' &= (-a/2, -a/\sqrt{12}, c/6) \\ \mathbf{c}' &= (a/2, -a/\sqrt{12}, c/6)\end{aligned}$$

Substitution of the values of a and c given above in terms of a_c confirms that in the cubic phase these vectors are orthogonal and of length a_c . The vector dot products of these three vectors give the angles between the vectors, which are all equal to $90^\circ - \epsilon$, where ϵ is the shear strain. The shear strains ϵ are shown in Figure 3c. Simple algebra shows, unsurprisingly, that the size of the shear strain ϵ is proportional to the difference $c/\sqrt{6} - a$.

Two points emerge from the calculation of the shear strain. The first is that there is very little variation with temperature, and the second is that there is a significant dependence on composition, which is the largest effect we can see here. It is clear that with increasing Sr composition the structure is becoming closer to a phase transition to a new structure of cubic metric, but the same transition is barely indicated on heating. Interestingly, the shear strain for the $x = 0$ case [7], which we plot in Appendix A, Figure A1a, shows a small increase on heating, which is unexpected but consistent with the overall temperature dependence of other symmetry-breaking distortions.

4.2. Atomic structure

4.2.1. Details of the crystal structure parameters. The Wyckoff positions of the basic Sr-doped BiFeO₃ structure in space group $R3c$, as shown in Figure 1, are given in Table 1, together with one representative example from our data. We also compare these with the sets of Wyckoff positions for the parent $R\bar{3}c$ and $Pm\bar{3}m$ phases. The relative displacements

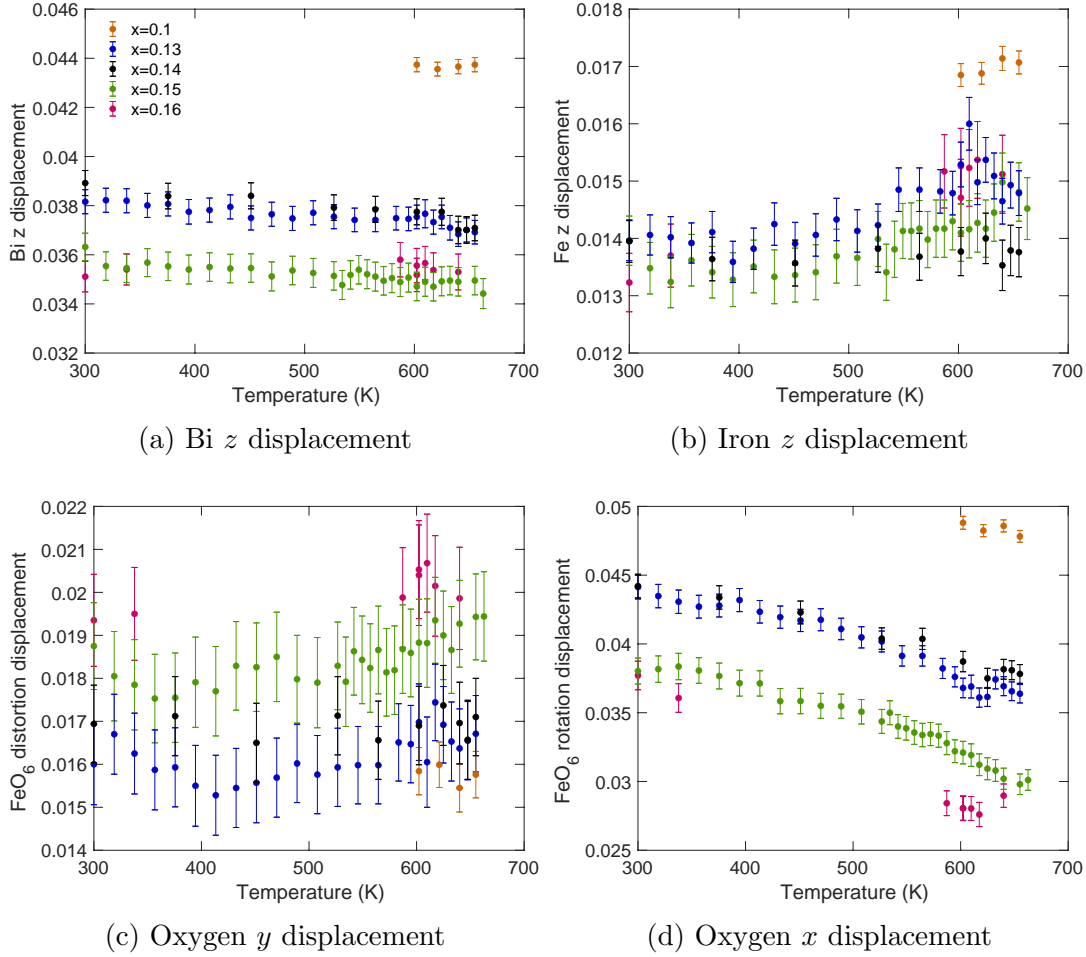


Figure 4: a,b) Variation of the two ferroelectric z axis displacements of $\text{Sr}_x\text{Bi}_{1-x}\text{FeO}_{3-x/2}$, iron $1/4 - z$ (a) and oxygen $1 - z$ (b), with temperature and chemical composition x . z is the fractional coordinate as obtained from Rietveld refinement c) Variation of the displacement of the oxygen atom, fractional coordinate y , that reflect the extent of expansion and contraction of the upper and lower (001) faces of the FeO_6 octahedra. d) Variation of the displacements of the oxygen atom, $1/2 - x$, where here x is the refined value of the fractional coordinate, which reflect the extent of FeO_6 octahedral rotation about [001]. The legend in plot (a) displays the values of composition x for each graph.

of the atoms along the z axis define the degree of ferroelectric distortion ($R\bar{3}c \rightarrow R3c$ transition). The displacement of the oxygen x fractional coordinate relative to the value $1/2$ in the parent cubic phase quantifies the extent of octahedral rotation ($Pm\bar{3}m \rightarrow R\bar{3}c$ transition). Finally, the displacement of the oxygen y fractional coordinate relative to value 0 in the parent cubic phase quantifies the extent to which the FeO_6 octahedra are distorted due to the ferroelectric atomic displacements, as discussed in the Introduction and as shown in Figure 1c. Refined values of the fractional atomic coordinates for iron (z) and oxygen (x, y, z), according to the space group $R\bar{3}c$ as given in Table 1, are given in the Supporting information [63] for all compositions and temperatures.

It is useful to note that the matrix to transform the lattice parameters from the cubic to rhombohedral setting in BiFeO₃ is

$$\mathbf{M} = \begin{pmatrix} 1 & 0 & -1 \\ -1 & 1 & 0 \\ 2 & 2 & 2 \end{pmatrix}$$

The matrix $(\mathbf{M}^{-1})^T$ then provides the transformation of fractional atomic coordinates from the cubic to rhombohedral settings.

4.2.2. Ferroelectric distortions. From the atomic structure and space group symmetry, as displayed in Figure 1a, it is clear that there are layers of each atom separated by $c/6$ along the z axis, which are associated with the ferroelectric polarisation.§ To analyse the ferroelectric distortions, we plot in Figure 4a the displacement of the Bi atom from the layer of oxygen atoms with which it would be coplanar in the parent $R\bar{3}c$ structure.|| This is actually calculated from the refined atomic coordinates of the oxygen atom as $1 - z$. Figures 1a and 1c show that there is also a displacement of the iron atom from the centre of the FeO₆ octahedra. The temperature dependence of the Fe z displacement relative to the centre of the two oxygen layers is shown in Figure 4b. Clearly, as seen in Figure 1a, the displacements of the Bi atoms relative to the planes of O atoms are larger than those of the Fe, by a factor of just over 2.5. Secondly, the ferroelectric displacements decrease with increased strontium content. On changing the Sr composition from $x = 0.1$ to $x = 0.16$ there is a reduction in the Bi cation displacement by a factor of 1.2. A similar reduction is seen for the Fe cation displacement, but the smaller overall size of the displacement means that the relative size of the errors is larger. Thirdly, there is only a weak dependence on temperature, although a small decrease in the Bi cation displacement can be seen for compositions $x = 0.13$ to 0.15. Any phase transition to the paraelectric phase must still be at much higher temperatures than were accessible in this study.

As noted before, and as seen in Figure 1 and in the comparison of Wyckoff positions given in Table 1, the z displacements of the Fe cations from the centre of the FeO₆ octahedra give contraction and expansion of the two faces parallel to the (001) planes rather than stretching and contracting the Fe–O bonds. This is seen directly as the value of the y fractional coordinate of the oxygen anion given in Table 1. Figure 4c shows the variation of the oxygen anion y displacements associated with the distortions of the octahedra. Whilst the values of the displacements as measured in fractional

§ For clarity, although ferroelectric polarisation hysteresis loops have been observed in similar samples of Sr-doped BiFeO₃ in work by the first author (ZM) [17], in this paper we consider ferroelectric distortions to be defined by the group-theoretical analysis of Aizu [67], based on the relationship between the symmetries of the parent and ferroelectric phase. Certainly the atomic displacements seen in both pure and Sr-doped BiFeO₃ are of the form that generate an *in-principle* reversible polarisation.

|| Although we set the Bi atom as the arbitrary origin in space group $R3c$, when we consider the ferroelectric atomic displacements along the z axis relative to the positions of the Bi atoms, we do not imply that the Bi atom has fixed position.

coordinates are similar in value to those of the Fe cation displacements, scaling by the lattice parameters indicates that whilst the Fe displacements are of a size up to 0.24 Å, the oxygen displacements are all lower than 0.11 Å. At first sight the data appear a little contradictory compared to Figures 4a and 4b in that the variation of the O anion displacements with Sr composition is not consistent with that of the cation displacements, but the relatively large size of the errors compared with the small size of the displacements may mean that systematic errors in the refinements have masked the expected behaviour. In any case, what is clear is that there is no significant variation in the oxygen displacements with temperature, consistent with the Bi and Fe ionic displacements.

4.2.3. Octahedral rotational distortions. The FeO₆ octahedral rotations associated with the change of space group symmetry from $Pm\bar{3}m$ to $R\bar{3}c$ is seen directly as the oxygen displacement in fractional coordinates $1/2 - x$, where the fractional coordinate x is given in Table 1. The results for this parameter from the Rietveld refinement are given in Figure 4d. The largest displacement is of size 0.27 Å ($\Delta x = 0.049$), in the case of strontium content $x = 0.1$, which corresponds to a rotation angle of 9.6°. As for the ferroelectric distortion, the rotation distortion is largest for smaller strontium content, but unlike the case of the ferroelectric distortion the octahedral rotations show more variation with temperature. This suggests that it might have been possible to see the transition to the phase having zero rotation on further heating. We will explore this possibility for other compositions in a later paper (in preparation).

4.2.4. Structural distortions and the lattice parameters. We can now explain the origin of the behaviour of the lattice parameters as seen in Figure 3a. The key point is that the value of lattice parameter a appears to have little variation with the strontium content, and conversely there is a large variation of c with composition, with larger values of c for lower strontium compositions. There are three main effects that change the lattice, namely creation of oxygen vacancies which will lower volume uniformly, the rotational distortion that mostly lowers the value of a , and the ferroelectric distortion that increases the value of c , at least to first order. This is illustrated in the graphic shown in Figure 5. Increasing Sr content in the first instance leads to a lowering of the values of both a and c relative to the values in the undoped sample with cubic metric, as represented by the horizontal broken line in the cartoon. The first distortion is associated with the rotations of the FeO₆ octahedra, which give the phase transition from $Pm\bar{3}m$ to $R\bar{3}c$ space groups. To first order, this will mostly affect the a lattice parameter, with a much smaller effect on the c lattice parameter. The change in a will be larger for smaller Sr content because, as seen in Figure 4d, the rotational transition is larger. Thus for a , one effect grows and the other shrinks on changing composition. It is therefore quite likely that the two competing effects are matched in a way that gives little overall variation of a with composition. On the other hand, for c , in addition to the effect of oxygen vacancies leading to volume reduction, the effect of the ferroelectric distortion will be

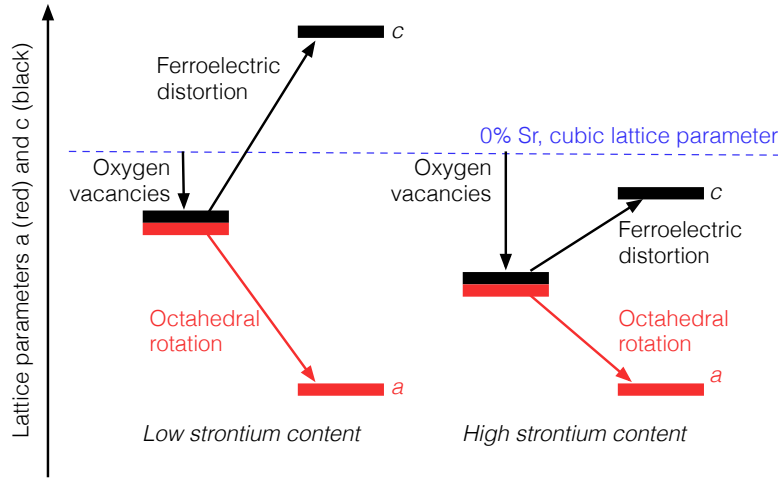


Figure 5: Representation of the changes in lattice parameters a (red) and c (black) in $\text{Sr}_x\text{Bi}_{1-x}\text{FeO}_{3-x/2}$ due to increased strontium content x . The graphic on the left shows the behaviour for low values of x , and the graphic on the right shows the behaviour for high values of x . The first effect is that of increased oxygen vacancies, which lowers the values of a and c relative to the values of the parent cubic phase for $x = 0$, which are shown as the horizontal blue dashed line. The values of the lattice parameters are reduced with increased x , the more so for larger values of x . The second effect is the rotations of the FeO_6 within the transition $Pm\bar{3}m \rightarrow R\bar{3}c$, which mostly reduces the size of a . Since the amplitude of rotation is larger for smaller x , this brings the values of a for low- x and high- x closer together since there is a balance of relative sizes of the two effects on a . The third effect is the ferroelectric transition, $R\bar{3}c \rightarrow R3c$, which primarily increases the value of c . This effect is larger for smaller x .

to increase the value of c . For low Sr content, the ferroelectric distortion is largest and the effect of oxygen vacancies is smallest, but at larger Sr content the effect of oxygen vacancies is largest and the effect of the ferroelectric distortion is smallest. This gives rise to a significant variation of the values of c .

4.2.5. Comparison with pure BiFeO_3 . To complete this section, we remark that the trends seen here are fully consistent with our data previously obtained on pure BiFeO_3 [7]. The analysis is given in Appendix A. We see similar trends in the variation with structure distortions in pure BiFeO_3 as seen in the doped samples. Moreover, the sizes of the distortions are all larger than seen for our samples with $x = 0.1$, consistent with the variations with composition observed in this study, and also with a recent x-ray diffraction measurement [38].

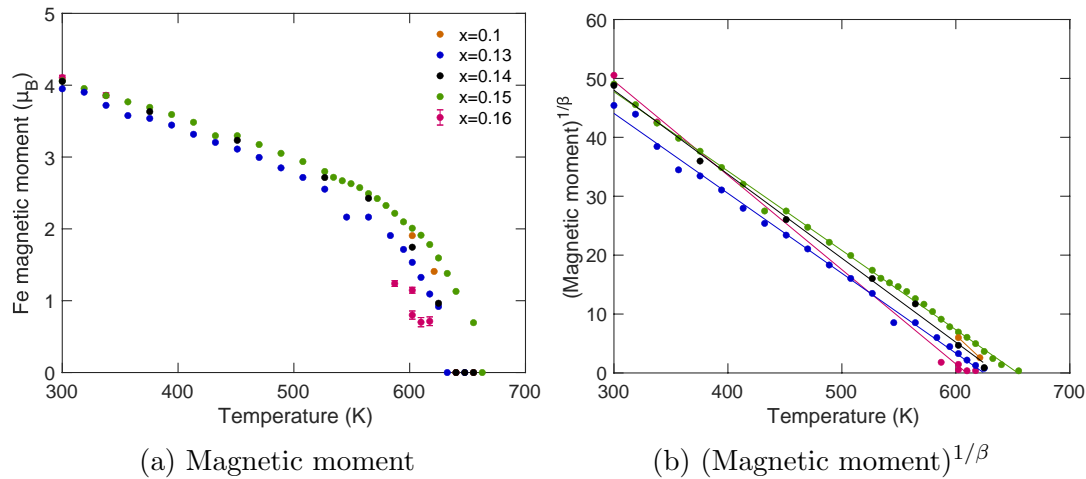


Figure 6: a) Temperature dependence of the iron sub-lattice magnetic moment associated with the antiferromagnetic order in $\text{Sr}_x\text{Bi}_{1-x}\text{FeO}_{3-x/2}$. b) Sublattice magnetic moment scaled to the power $1/\beta$ where $\beta = 0.36$. The lines show an indicative linear function to demonstrate the scaling relation $M \propto (T_c - T)^\beta$. The legend in plot (a) displays the values of composition x for both graphs.

4.3. Antiferromagnetic order

As noted above, the antiferromagnetic order is of G-type. The refined values of the atomic moment on the iron cation are shown in Figure 6a. It can be seen that the magnetic moments are similar for all compositions at a temperature of 300 K, indeed with no obvious variation with chemical composition. The average antiferromagnetic moments decrease with temperature in each composition with a second-order phase transition at temperatures between 600–650 K. The actual transition temperatures have a low level of consistency with composition (discussed below), which reflects the limitations in the accuracy of the absolute thermometry in the experiments.

Given that the spin state of the Fe^{3+} cation is $5/2$, the spin ordering can be reasonably well approximated by the three-dimensional Heisenberg model. In this case, the sub-lattice moment will vary as $M \propto (T_c - T)^\beta$, with $\beta \simeq 0.36$ [68]. Thus in Figure 6b we plot $M^{1/\beta}$ against temperature, and we show fitted straight lines for the different compositions. The data follow this relation over a remarkably wide range of temperatures within statistical accuracy.

The important point to note is that the antiferromagnetic phase transition appears to be largely independent of chemical composition, which we now discuss. It is useful to compare our results with those of a recent neutron powder diffraction study of the BiFeO_3 – CaTiO_3 solid solution for 0–25% Ca/Ti content, and of one sample within the BiFeO_3 – BaTiO_3 solid solution for 15% Ba/Ti content, at room temperature [57]. There are two key differences between our study and this recent study aside from the fact that we included temperature variation. First is that in the BiFeO_3 –titanate solid solutions

there is progressive substitution of the Fe sites, whereas in Sr-doped BiFeO₃ the number of Fe ions remains constant. The second is that in the BiFeO₃–titanate solid solutions there are no oxygen vacancies whereas the doping of BiFeO₃ leads to the formation of charge-balancing oxygen vacancies since there appears to be no conversion of Fe³⁺ to Fe²⁺ [14].

In the BiFeO₃–titanate solid solutions there is a reduction of magnetisation on increasing the titanate content. From the data [57] it appears that this matches very closely the replacement of Fe cations by the non-magnetic titanium cations. On the other hand, the magnetisation in our data is only very weakly dependent on the strontium content. If we consider the four samples at room temperature for strontium composition $x = 0.13\text{--}0.16$ we find magnetisation per atom (in units of Bohr magnetons) of 3.95(3), 4.054(3), 4.06(3) and 4.11(3) respectively (errors in brackets, data are in the Supporting Information [63]). Thus within error Sr-doped BiFeO₃ shows a very slight increase in magnetisation on increasing x , which would indicate a commensurable slight increase in the magnetic ordering temperature with increasing x . Noting the caveat given above regarding the limitations of thermometry, the data are consistent with this prediction for the cases where the measurements followed the same heating history ($x = 0.13\text{--}0.15$). The effect however is small compared with the structural changes, both polarisation displacements and octahedral rotations. ¶

The variation of the ionic displacements causing polarisation by similar amounts across the range of compositions in the BiFeO₃–titanate solution solutions as in Sr-doped BiFeO₃. However, in the BiFeO₃–titanate solution solutions the displacements associated with octahedral rotations change very little, which is not surprising given that CaTiO₃ has similar tilts to BiFeO₃, but in Sr-doped BiFeO₃ there is a reduction in the size of the octahedral tilt that is larger (relatively) than the reduction in the polarisation. Taking account of all these differences, and noting the point about the magnetisation in the BiFeO₃–titanate solution solutions changing only with the iron content, we can draw the conclusion than in spite of the structural changes BiFeO₃ systems, the antiferromagnetic phase transition is largely independent of chemical composition, and thus independent of the extent of ferroelectricity and of the extent of the octahedral rotation distortion.

5. Conclusions

Much of the analysis of this paper concerns a detailed characterisation, using neutron powder diffraction and Rietveld refinement, of the effects of the doping of the multiferroic material BiFeO₃ by strontium. We have studied three main distortions of the structure, namely those associated with the rotational instability that drives the distortion from $Pm\bar{3}m$ to $R\bar{3}m$ space groups, the ferroelectric deformation that lowers the symmetry

¶ It is important to note that doping BiFeO₃ with Sr generates vacancies on the oxygen sites. However, the proportion of oxygen lost is 1/6 of the Sr composition, so for Sr content $x = 0.1$ the oxygen content per site has only fallen to 0.983. This will have a very small disruption of the percolation of the magnetic Fe–O–Fe super-exchange pathways.

further to space group $R3c$, and the antiferromagnetic phase transition.

The structural instabilities appear to have only a very weak dependence on temperature, although the rotational deformation shows a slight decrease with increasing temperature for higher strontium content. On the other, there is an appreciable variation of both deformations with chemical composition, together with the associate lattice shear strain. This variation with composition is consistent with a possible phase transition to a phase of cubic symmetry (space group $Pm\bar{3}m$) for slightly higher Sr content. The antiferromagnetism for all compositions shows a normal temperature dependence up to the phase transition, with a variation consistent with the scaling relationship for the three-dimensional Heisenberg model. There is not a significant variation for the antiferromagnetic phase transition with composition, nor of the absolute values of the magnetic moments at ambient temperature.

From the detailed characterisation presented in this paper emerges a significant conclusion, that there appears to be virtually no sign of any correlation between the antiferromagnetic order and the structural deformations in Sr-doped BiFeO₃, most pertinent of which, for the discussion of multiferroic properties, is the ferroelectricity. Thus it appears that the two different ferroic components of BiFeO₃ have no significant correlations with each other, nor with the rotational distortions.

Acknowledgements

We are grateful to China Spallation Neutron Source for provision of beam time (experiment proposal number P2018091000001). ZM, LT and MTD acknowledge support from the National Natural Science Foundation of China (grant reference 12174274). MTD would like to thank Robert von Dreele for giving some very useful advice in the use of GSAS-II. And of course, we are very grateful to him for the existence of GSAS!

Appendix A. Comparison with data for pure bismuth ferrite

It is interesting to compare the results presented here with those for pure BiFeO₃ in our recent study [7]. We present in this Appendix results from that study – referred here as Du – that correspond to those reported above. Lattice parameters are published in Du and are not reproduced here.

In comparison with the lattice parameter data presented in Figure 3a, the values of $a/\sqrt{2}$ published in Du covers the range 3.945–3.967 Å for temperatures 300–800 K, and for $c/\sqrt{12}$ the corresponding range of values are 4.004–4.032 Å. These data match the trends of both thermal expansion and the fact that the value of $a/\sqrt{2}$ is part of the same cluster of values for all strontium composition, and the value of $c/\sqrt{12}$ lies above the value for $x = 0.1$ consistent with the variation with composition seen in Figure 3a.

The shear strain from the data of Du, shown in Figure A1a, follows the trend of Figure 3c, although showing a very slight increase on heating. The values of the strain angle lie above the data for Sr-doped BiFeO₃, exactly in line with the trends in the

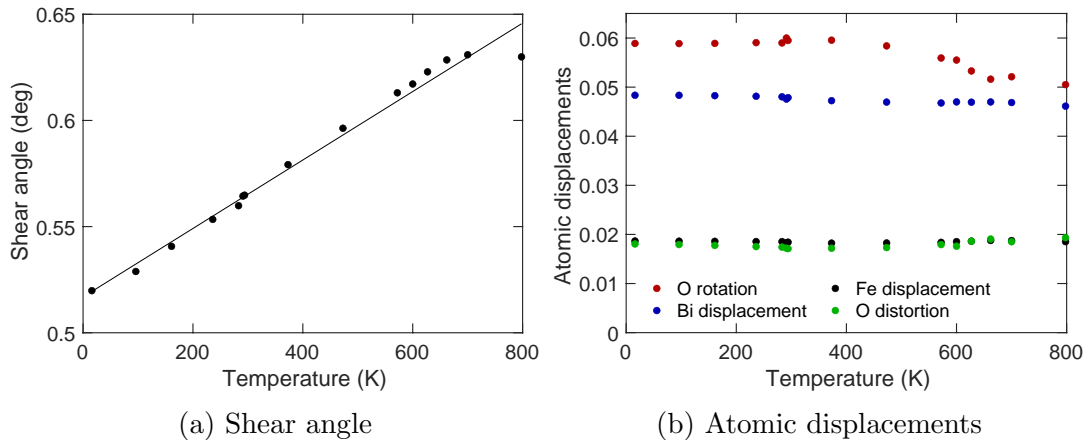


Figure A1: a) Temperature dependence of the lattice shear angle of pure BiFeO_3 from the data of Du [7], for comparison with Figure 3c. b) Temperature dependence of the displacements of atomic fractional coordinates in pure BiFeO_3 , with z displacements relative to the Bi atom being chosen as the origin. These data should be compared with the new data for Sr-doped BiFeO_3 presented in Figure 4.

data shown in Figure 3c that show that strain angle decreases for increasing strontium content, and is therefore maximum in the pure BiFeO_3 .

In Figure A1b we plot the four atomic displacements, in terms of fractional coordinates, namely $\text{Fe } 1/4 - z$ and $\text{O } 1/2 - x, y, 1 - z$. These data and the data presented in Figure 4 are consistent. The weak temperature dependence seen for all data sets in Figure A1b is exactly as seen for the range of data for the strontium doped materials in Figure 4. Furthermore, the values of atomic displacements for the ferroelectric and octahedral rotation distortions are all consistent with the data in Figure 4. In each case the values for pure BiFeO_3 are slightly greater than for $x = 1$ in $\text{Sr}_x\text{Bi}_{1-x}\text{FeO}_{3-x/2}$.

References

- [1] Donna C Arnold, Kevin S Knight, Finlay D Morrison, and Philip Lightfoot. Ferroelectric-Paraelectric Transition in BiFeO_3 : Crystal Structure of the Orthorhombic β Phase. *Physical Review Letters*, 102:027602, 2009.
- [2] A Palewicz, I Sosnowska, R Przeniosło, and A W Hewat. BiFeO_3 Crystal Structure at Low Temperatures. *Acta Physica Polonica A*, 117:296–301, 2010.
- [3] Gustau Catalan and James F Scott. Physics and applications of bismuth ferrite. *Advanced Materials*, 21:2463–2485, 2009.
- [4] Je-Geun Park, Manh Duc Le, Jaehong Jeong, and Sanghyun Lee. Structure and spin dynamics of multiferroic BiFeO_3 . *Journal of Physics: Condensed Matter*, 26:433202, 2014.
- [5] Christopher J. Howard and Harold T. Stokes. Structures and phase transitions in perovskites – a group-theoretical approach. *Acta Crystallographica Section A*, 61:93–111, 2005.
- [6] Donna C Arnold, Kevin S Knight, Gustau Catalan, Simon A T Redfern, James F Scott, Philip Lightfoot, and Finlay D Morrison. The β -to- γ Transition in BiFeO_3 : A Powder Neutron Diffraction Study. *Advanced Functional Materials*, 20:2116–2123, 2010.
- [7] Juan Du, Anthony E Phillips, Donna C Arnold, David A Keen, Matthew G Tucker, and Martin T

- Dove. Structural study of bismuth ferrite BiFeO₃ by neutron total scattering and the reverse Monte Carlo method. *Physical Review*, 100:104111, 2019.
- [8] V.A. Khomchenko, D.A. Kiselev, M. Kopcewicz, M. Maglione, V.V. Shvartsman, P. Borisov, W. Kleemann, A.M.L. Lopes, Y.G. Pogorelov, J.P. Araujo, R.M. Rubinger, N.A. Sobolev, J.M. Vieira, and A.L. Kholkin. Doping strategies for increased performance in BiFeO₃. *Journal of Magnetism and Magnetic Materials*, 321:1692–1698, 2009.
- [9] Rajata Kumar Mansingh, Raj Kishore Mishra, and Tapan Dash. Modifying BiFeO₃ (BFO) for multifunctional applications - a review. *AIP Conference Proceedings*, 2417:020021, 2021.
- [10] Alexandra S. Gibbs, Donna C. Arnold, Kevin S. Knight, and Philip Lightfoot. High-temperature phases of multiferroic BiFe_{0.7}Mn_{0.3}O₃. *Physical Review B*, 87:224109, 2013.
- [11] Donna C Arnold. Composition-driven structural phase transitions in rare-earth-doped BiFeO₃ ceramics: a review. *IEEE Transactions on Ultrasonics, Ferroelectrics, and Frequency Control*, 62:62–82, 2015.
- [12] M A Carpenter, C J Howard, K S Knight, and Z Zhang. Structural relationships and a phase diagram for (Ca,Sr)TiO₃ perovskites. *Journal of Physics: Condensed Matter*, 18:10725–10749, 2006.
- [13] I. O. Troyanchuk, M. V. Bushinsky, D. V. Karpinsky, V. Sirenko, V. Sikolenko, and V. Efimov. Structural and magnetic phases of Bi_{1-x}A_xFeO_{3-δ} (A = Sr, Pb) perovskites. *The European Physical Journal B*, 73:375–381, 2010.
- [14] E. Folcke, J.M. Le Breton, Y. Bréard, and A. Maignan. Mössbauer spectroscopic analysis of Bi_{1-x}Sr_xFeO_{3-δ} perovskites. *Solid State Sciences*, 12:1387–1392, 2010.
- [15] Dinesh Varshney and Ashwini Kumar. Structural, Raman and dielectric behavior in Bi_{1-x}Sr_xFeO₃ multiferroic. *Journal of Molecular Structure*, 1038:242–249, 2013.
- [16] Manisha Rangi, Ashish Agarwal, Sujata Sanghi, Ripandeep Singh, S. S. Meena, and A. Das. Crystal structure and magnetic properties of Bi_{0.8}A_{0.2}FeO₃ (A = La, Ca, Sr, Ba) multiferroics using neutron diffraction and Mossbauer spectroscopy. *AIP Advances*, 4:087121, 2014.
- [17] Zheng-Zheng Ma, Jian-Qing Li, Zi-Peng Chen, Zhao-Ming Tian, Xiao-Jun Hu, and Hai-Jun Huang. Multiferroic properties and exchange bias in Bi_{1-x}Sr_xFeO₃ (x = 0–0.6) ceramics. *Chinese Physics B*, 23:097505, 2014.
- [18] F. Pedro-García, A.M. Bolarín-Miró, F. Sánchez-De Jesús, C.A. Cortés-Escobedo, Z. Valdez-Nava, and G. Torres-Villaseñor. Stabilization of α-BiFeO₃ structure by Sr²⁺ and its effect on multiferroic properties. *Ceramics International*, 44:8087–8093, 2018.
- [19] David C Palmer. Visualization and analysis of crystal structures using CrystalMaker software. *Zeitschrift für Kristallographie - Crystalline Materials*, 230:559–572, 2015.
- [20] J.M. Moreau, C. Michel, R. Gerson, and W.J. James. Ferroelectric BiFeO₃ x-ray and neutron diffraction study. *Journal of Physics and Chemistry of Solids*, 32:1315–1320, 1971.
- [21] C.N.W. Darlington and H.D. Megaw. The low-temperature phase transition of sodium niobate and the structure of the low-temperature phase, N. *Acta Crystallographica Section B: Structural Crystallography and Crystal Chemistry*, 29:2171–2185, 1973.
- [22] A M Glazer. The classification of tilted octahedra in perovskites. *Acta Crystallographica B*, 28:3384–3392, 1972.
- [23] G. Marschick, J. Schell, B. Stöger, J. N. Gonçalves, M. O. Karabasov, D. Zyabkin, A. Welker, M. Escobar C., D. Gärtner, I. Efe, R. A. Santos, J. E. M. Laulainen, and D. C. Lupascu. Multiferroic bismuth ferrite: Perturbed angular correlation studies on its ferroic α–β phase transition. *Physical Review B*, 102:224110, 2020.
- [24] R. Palai, R. S. Katiyar, H. Schmid, P. Tissot, S. J. Clark, J. Robertson, S. A. T. Redfern, G. Catalan, and J. F. Scott. β phase and γ–β metal-insulator transition in multiferroic BiFeO₃. *Physical Review B*, 77:014110, 2008.
- [25] Antonio Perejón, Pedro E. Sánchez-Jiménez, José M. Criado, and Luis A. Pérez-Maqueda. Thermal stability of multiferroic BiFeO₃: Kinetic nature of the β–γ transition and peritectic decomposition. *The Journal of Physical Chemistry C*, 118:26387–26395, 2014.

- [26] E. O. Wollan and W. C. Koehler. Neutron diffraction study of the magnetic properties of the series of perovskite-type compounds $[(1-x)\text{La}, x\text{Ca}]\text{MnO}_3$. *Physical Review*, 100:545–563, 1955.
- [27] I Sosnowska, T P Neumaier, and E Steichele. Spiral magnetic ordering in bismuth ferrite. *Journal of Physics C: Solid State Physics*, 15:4835–4846, 1982.
- [28] Julia Herrero-Albillos, Gustau Catalan, José Alberto Rodríguez-Velamazán, Michel Viret, Dorothée Colson, and James F Scott. Neutron diffraction study of the BiFeO₃ spin cycloid at low temperature. *Journal of Physics: Condensed Matter*, 22:256001, 2010.
- [29] M Ramazanoglu, M Laver, W Ratcliff, S M Watson, W C Chen, A Jackson, K Kothapalli, Seongsu Lee, S W Cheong, and V Kiryukhin. Local Weak Ferromagnetism in Single-Crystalline Ferroelectric BiFeO₃. *Physical Review Letters*, 107:207206, 2011.
- [30] D. Rahmedov, Dawei Wang, Jorge Íñiguez, and L. Bellaiche. Magnetic cycloid of BiFeO₃ from atomistic simulations. *Physical Review Letters*, 109:037207, 2012.
- [31] I. Dzyaloshinsky. A thermodynamic theory of “weak” ferromagnetism of antiferromagnetics. *Journal of Physics and Chemistry of Solids*, 4:241–255, 1958.
- [32] Tôru Moriya. Anisotropic superexchange interaction and weak ferromagnetism. *Physical Review*, 120:91–98, 1960.
- [33] P. Hermet, M. Goffinet, J. Kreisel, and Ph. Ghosez. Raman and infrared spectra of multiferroic bismuth ferrite from first principles. *Physical Review B*, 75:220102, 2007.
- [34] J. Hlinka, J. Pokorný, S. Karimi, and I. M. Reaney. Angular dispersion of oblique phonon modes in BiFeO₃ from micro-Raman scattering. *Physical Review B*, 83:020101, 2011.
- [35] O. Delaire, M. B. Stone, J. Ma, A. Huq, D. Gout, C. Brown, K. F. Wang, and Z. F. Ren. Anharmonic phonons and magnons in BiFeO₃. *Physical Review B*, 85:064405, 2012.
- [36] John A. Schneeloch, Zhijun Xu, Jinsheng Wen, P. M. Gehring, C. Stock, M. Matsuda, B. Winn, Genda Gu, Stephen M. Shapiro, R. J. Birgeneau, T. Ushiyama, Y. Yanagisawa, Y. Tomioka, T. Ito, and Guangyong Xu. Neutron inelastic scattering measurements of low-energy phonons in the multiferroic BiFeO₃. *Physical Review B*, 91:064301, 2015.
- [37] Zhijun Xu, Jinsheng Wen, Tom Berlijn, Peter M. Gehring, Christopher Stock, M. B. Stone, Wei Ku, Genda Gu, Stephen M. Shapiro, R. J. Birgeneau, and Guangyong Xu. Thermal evolution of the full three-dimensional magnetic excitations in the multiferroic BiFeO₃. *Physical Review B*, 86:174419, 2012.
- [38] Mariusz Lejman, Charles Paillard, Vincent Juvé, Gwenaëlle Vaudel, Nicolas Guiblin, Laurent Bellaiche, Michel Viret, Vitaliy E. Gusev, Brahim Dkhil, and Pascal Ruello. Magnetoelastic and magnetoelectric couplings across the antiferromagnetic transition in multiferroic BiFeO₃. *Physical Review B*, 99:104103, 2019.
- [39] J. B. Neaton, C. Ederer, U. V. Waghmare, N. A. Spaldin, and K. M. Rabe. First-principles study of spontaneous polarization in multiferroic BiFeO₃. *Physical Review B*, 71:014113, 2005.
- [40] Claude Ederer and Nicola A. Spaldin. Weak ferromagnetism and magnetoelectric coupling in bismuth ferrite. *Physical Review B*, 71:060401, 2005.
- [41] Silvia Picozzi and Claude Ederer. First principles studies of multiferroic materials. *Journal of Physics: Condensed Matter*, 21:303201, 2009.
- [42] Ifflah Laraib, Marciano A. Carneiro, and Anderson Janotti. Untangling the effects of octahedral rotation and ionic displacements on the electronic structure of BiFeO₃. *Physical Review B*, 104:035159, 2021.
- [43] Shi Liu, Ilya Grinberg, and Andrew M Rappe. Development of a bond-valence based interatomic potential for BiFeO₃ for accurate molecular dynamics simulations. *Journal of Physics: Condensed Matter*, 25:102202, 2013.
- [44] P. Ravindran, R. Vidya, A. Kjekshus, H. Fjellvåg, and O. Eriksson. Theoretical investigation of magnetoelectric behavior in BiFeO₃. *Physical Review B*, 74:224412, 2006.
- [45] D Sando, A Barthélémy, and M Bibes. BiFeO₃ epitaxial thin films and devices: past, present and future. *Journal of Physics: Condensed Matter*, 26:473201, 2014.
- [46] Jan-Chi Yang, Qing He, Pu Yu, and Ying-Hao Chu. BiFeO₃ thin films: A playground for exploring

- electric-field control of multifunctionalities. *Annual Review of Materials Research*, 45:249–275, 2015.
- [47] Li Yin and Wenbo Mi. Progress in BiFeO₃-based heterostructures: materials, properties and applications. *Nanoscale*, 12:477–523, 2020.
- [48] Carlos Gumiel and David G. Calatayud. Thin film processing of multiferroic BiFeO₃: From sophistication to simplicity. a review. *Boletín de la Sociedad Española de Cerámica y Vidrio*, 2021.
- [49] Joel Bertinshaw, Ronald Maran, Sara J. Callori, Vidya Ramesh, Jeffery Cheung, Sergey A. Danilkin, Wai Tung Lee, Songbai Hu, Jan Seidel, Nagarajan Valanoor, and Clemens Ulrich. Direct evidence for the spin cycloid in strained nanoscale bismuth ferrite thin films. *Nature Communications*, 7:12664, 2016.
- [50] Bhagwati Prasad, Yen-Lin Huang, Rajesh V. Chopdekar, Zuhuang Chen, James Steffes, Sujit Das, Qian Li, Mengmeng Yang, Chia-Ching Lin, Tanay Gosavi, Dmitri E. Nikonov, Zi Qiang Qiu, Lane W. Martin, Bryan D Huey, Ian Young, Jorge Íñiguez, Sasikanth Manipatruni, and Ramamoorthy Ramesh. Ultralow voltage manipulation of ferromagnetism. *Advanced Materials*, 32:2001943, 2020.
- [51] Stuart R. Burns, Oliver Paull, Jean Juraszek, Valanoor Nagarajan, and Daniel Sando. The experimentalist’s guide to the cycloid, or noncollinear antiferromagnetism in epitaxial BiFeO₃. *Advanced Materials*, 32:2003711, 2020.
- [52] W. Ratcliff, Zahra Yamani, V. Anbusathaiah, T. R. Gao, P. A. Kienzle, H. Cao, and I. Takeuchi. Electric-field-controlled antiferromagnetic domains in epitaxial BiFeO₃ thin films probed by neutron diffraction. *Physical Review B*, 87:140405, 2013.
- [53] Chia-Ching Lin, Tanay Gosavi, Dmitri Nikonov, Yen-Lin Huang, Bhagwati Prasad, WonYoung Choi, Van Tuong Pham, Inge Groen, Jun-Yang Chen, Mahendra D. C., Huichu Liu, Kaan Oguz, Emily S. Walker, John Plombon, Benjamin Buford, Carl H. Naylor, Jian-Ping Wang, Felix Casanova, Ramamoorthy Ramesh, and Ian A. Young. Experimental demonstration of integrated magneto-electric and spin-orbit building blocks implementing energy-efficient logic. In *2019 IEEE International Electron Devices Meeting (IEDM)*, pages 37.3.1–37.3.4, 2019.
- [54] J. T. Heron, M. Trassin, K. Ashraf, M. Gajek, Q. He, S. Y. Yang, D. E. Nikonov, Y-H. Chu, S. Salahuddin, and R. Ramesh. Electric-field-induced magnetization reversal in a ferromagnet-multiferroic heterostructure. *Physical Review Letters*, 107:217202, 2011.
- [55] Tim P. Comyn, Tim Stevenson, Maisoon Al-Jawad, Stuart L. Turner, Ronald I. Smith, Andrew J. Bell, and Robert Cywinski. High temperature neutron diffraction studies of 0.9BiFeO₃-0.1PbTiO₃. *Journal of Applied Physics*, 105:094108, 2009.
- [56] Izabela Sosnowska, Masaki Azuma, Radosław Przeniosło, Dariusz Wardecki, Wei-tin Chen, Kengo Oka, and Yuichi Shimakawa. Crystal and magnetic structure in co-substituted BiFeO₃. *Inorganic Chemistry*, 52:13269–13277, 2013.
- [57] V. A. Khomchenko, D. V. Karpinsky, S. I. Latushka, A. Franz, V. V. Sikolenko, S. V. Dubkov, M. V. Silibin, and J. A. Paixão. The structural origin of composition-driven magnetic transformation in BiFeO₃-based multiferroics: a neutron diffraction study. *Journal of Materials Chemistry C*, 7:6085–6090, 2019.
- [58] Lucangelo Dimesso. Pechini processes: An alternate approach of the sol-gel method, preparation, properties, and applications. In Lisa Klein, Mario Aparicio, and Andrei Jitianu, editors, *Handbook of Sol-Gel Science and Technology*, pages 1–22. Springer International Publishing, Cham, 2016.
- [59] Z. M. Tian, S. L. Yuan, X. F. Zheng, L. C. Jia, S. X. Huo, H. N. Duan, and L. Liu. Spin-glasslike behavior and exchange bias in multiferroic bi1/3sr2/3feo3 ceramics. *Applied Physics Letters*, 96:142516, 2010.
- [60] Jie Chen, Le Kang, Huaile Lu, Ping Luo, Fangwei Wang, and Lunhua He. The general purpose powder diffractometer at CSNS. *Physica B: Physics of Condensed Matter*, 551:370–372, 2018.
- [61] Lunhua He, Jie Chen, Huaile Lu, Ping Luo, Yaoda Wu, Le Kang, Jiuchang Zhang, Junrong Zhang, Rong Du, Xuejun Jia, Tianjiao Liang, and Fangwei Wang. First experimental results from the

- GPPD diffractometer at the CSNS. *Neutron News*, 29:7–10, 2018.
- [62] Brian H Toby and Robert B Von Dreele. GSAS-II: the genesis of a modern open-source all purpose crystallography software package. *Journal of Applied Crystallography*, 46:544–549, 2013.
- [63] ZhengZheng Ma et al. Supporting information. <http://something>.
- [64] Michael A Carpenter, Ana I Becerro, and Friedrich Seifert. Strain analysis of phase transitions in (Ca,Sr)TiO₃ perovskites. *American Mineralogist*, 86:348–363, 2001.
- [65] Ruth E A McKnight, C J Howard, and M A Carpenter. Elastic anomalies associated with transformation sequences in perovskites: I. Strontium zirconate, SrZrO₃. *Journal of Physics: Condensed Matter*, 21:015901–15, 2008.
- [66] R. D. Shannon. Revised effective ionic radii and systematic studies of interatomic distances in halides and chalcogenides. *Acta Crystallographica Section A*, 32:751–767, 1976.
- [67] Kêitsiro Aizu. Possible species of ferromagnetic, ferroelectric, and ferroelastic crystals. *Physical Review B*, 2:754–772, 1970.
- [68] Christian Holm and Wolfhard Janke. Critical exponents of the classical three-dimensional Heisenberg model: A single-cluster Monte Carlo study. *Physical Review B*, 48:936–950, 1993.